Seasonal Variability of the Gulf Stream Kinetic Energy

DUJUAN KANG AND ENRIQUE N. CURCHITSER

Department of Environmental Sciences, Rutgers, The State University of New Jersey, New Brunswick, New Jersey

ANTHONY ROSATI

NOAA/Geophysical Fluid Dynamics Laboratory, Princeton, New Jersey

(Manuscript received 1 December 2015, in final form 8 February 2016)

ABSTRACT

The seasonal variability of the mean kinetic energy (MKE) and eddy kinetic energy (EKE) of the Gulf Stream (GS) is examined using high-resolution regional ocean model simulations. A set of three numerical experiments with different surface wind and buoyancy forcing is analyzed to investigate the mechanisms governing the seasonal cycle of upper ocean energetics. In the GS along-coast region, MKE has a significant seasonal cycle that peaks in summer, while EKE has two comparable peaks in May and September near the surface; the May peak decays rapidly with depth. In the off-coast region, MKE has a weak seasonal cycle that peaks in summer, while EKE has a dominant peak in May and a secondary peak in September near the surface. The May peak also decays with depth leaving the September peak as the only seasonal signal below 100 m. An analysis of the three numerical experiments suggests that the seasonal variability in the local wind forcing significantly impacts the September peak of the along-coast EKE through a local-flow barotropic instability process. Alternatively, the seasonal buoyancy forcing primarily impacts the flow baroclinic instability and is consequently related to the May peak of the upper ocean EKE in both regions. The analysis results indicate that the seasonal cycle of the along-coast MKE is influenced by both local energy generation by wind and the advection of energy from upstream regions. Finally, the MKE cycle and the September peak of EKE in the off-coast region are mainly affected by advection of energy from remote regions, giving rise to correlations with the seasonal cycle of remote winds.

1. Introduction

The Gulf Stream (GS) and associated eddies play an important role in distributing the energy, momentum, and biogeochemical properties in the northwest Atlantic Ocean (e.g., The Ring Group 1981; Hogg 1992; Ryan et al. 2001). Significant seasonal variability has been observed in the GS position, transport, and eddy kinetic energy (EKE) field; however, the dynamics governing the variability are not fully understood (e.g., Worthington 1976; Fu et al. 1987; Ezer and Mellor 1992; Garnier and Schopp 1999; Brachet et al. 2004; Zhai et al. 2008; Rossby et al. 2010; Kang and Curchitser 2013).

Wind was indicated as a major force driving upper ocean circulation and affecting the eddy activity either directly by local generation of EKE or indirectly by influencing flow instabilities (Gill et al. 1974; Garnier and Schopp 1999; Stammer and Wunsch 1999; Stammer et al. 2001). The role of wind forcing on the eddy variability is spatially variable. Early studies using stochastic models suggested that the eddies are primarily generated by fluctuating winds in regions of weak eddy activity (Frankignoul and Müller 1979; Müller and Frankignoul 1981). In subsequent observational studies, a significant correlation was found between the seasonal cycles of EKE and local wind stress in the northern North Atlantic, where the background EKE level is low (White and Heywood 1995; Stammer and Wunsch 1999). In regions of high EKE level, such as the GS region, it is difficult to determine which of the two mechanisms (direct local generation vs indirect influences by winds) is more important. It has been found that the seasonal cycle of the GS has different phases at different locations (Stommel 1965). In the Florida Straits, the GS transport variability peaks in summer (Niiler and

Corresponding author address: Dujuan Kang, Department of Environmental Sciences, Rutgers University, 14 College Farm Rd., New Brunswick, NJ 08901.
E-mail: dujuan@esm.rutgers.edu

DOI: 10.1175/JPO-D-15-0235.1

Richardson 1973), which seems to be related to the seasonal local wind stress that also peaks in summer. It has been suggested that such seasonality in the Florida Current is forced by wind stress and remote baroclinic signals passing over the varying bottom topography (Anderson and Corry 1985). Yang (2015) pointed out that the seasonal variability of transport at 26.5°N is related to the adjustment to basinwide wind stress. In the GS region downstream of Cape Hatteras, the local wind forcing has an annual cycle that peaks in late winter and early spring (Fu et al. 1987; Brachet et al. 2004). The seasonal cycle of the surface EKE in this region was found to lag the wind cycle by a couple of months (Garnier and Schopp 1999; Zhai et al. 2008; Kang and Curchitser 2013). Some studies suggested that the EKE variability in the GS region is mainly related to the flow instability instead of the direct wind generation (Frankignoul and Müller 1979; LeTraon et al. 1990).

Thermal forcing was also suggested as an influence to the seasonal variability of the eddy activity (Gill et al. 1974; Csanady 1982; Qiu 1999; Chaigneau et al. 2008). Local heating/cooling can change the density structure in the top few hundred meters and hence affect the stability properties of the ocean (Gill et al. 1974). In the GS region downstream of Cape Hatteras, the upper ocean is well stratified in summer/early autumn due to strong surface heating and weak wind-induced vertical mixing. As the cooling-induced convection and wind-induced vertical mixing are enhanced in winter, the thermocline starts to tilt and reaches the maximum steepness in early spring, indicating that the flow is the most baroclinically unstable during this season. In late spring, the isotherms start to flatten and then in summer form a shallow and flat thermocline. Such an annual cycle of the vertical thermal structure was observed across the GS along both 60°W and 65°W based on the *World Ocean Atlas* (Zhai et al. 2008) and the regional ocean model simulation (Kang and Curchitser 2013), respectively. The seasonal cycle of the surface EKE in this region lags the cycle of baroclinic instability by 2–3 months. It has been suggested that the large amount of available potential energy (APE) built up during winter/early spring is released by eddies in late spring when the isotherms are flattening to form the thermocline in summer (Kang and Curchitser 2013). A similar correlation between surface EKE and the baroclinic instability was also observed in the North Pacific (Qiu 1999) and the southern Indian Ocean (Jia and Wu 2011) who employed a theoretical model to show that the lag of a couple of months corresponds to the length of time for unstable waves to fully grow in the respective regions.

Stammer and Wunsch (1999) and Stammer et al. (2001) suggested that bottom topography can impact eddy variability. In the northwest Atlantic, the interaction between the GS and the New England Seamount Chain (NESC) has been shown to affect the GS meandering and eddy activity (Spall and Robinson 1990; Teague and Hallock 1990). It was also found that the seasonal variability of the GS position is more pronounced in the NESC region (Kang and Curchitser 2013). The seasonally varying GS position may influence the GS–NESC interaction and is consequently related to the eddy variability in this region.

In addition, the dissipation mechanism was proposed to explain the seasonal variability of surface EKE in the GS extension region (Zhai et al. 2008). It was suggested that the higher EKE in summer is due to the capping of summer thermocline that shields eddies from thermal interaction with the atmosphere (Zhai and Greatbatch 2006). Likewise, the lower EKE in winter might be related to the strong mechanical damping of eddies by the winter wind (Duhaut and Straub 2006).

In this study, we focus on investigating the influence of surface wind and buoyancy forcing on the GS seasonality. We employ high-resolution regional ocean model simulations to examine the seasonal variability of the kinetic energy (KE) for monthly mean and monthly varying flows in two GS subdomains upstream and downstream of Cape Hatteras. We perform a set of three numerical experiments with different surface wind and buoyancy forcing in order to study their direct and indirect impacts on the seasonality of KE energetics in both GS regions. Results of these experiments are analyzed based on the energy analysis framework presented in Kang and Curchitser (2015). Moreover, we apply our analysis throughout the upper 500 m of the water column in order to obtain a three-dimensional picture of the upper ocean KE energetics and the governing dynamics. The rest of the paper is organized as follows: section 2 describes the analysis framework for the monthly mean and monthly varying KE used in this study, section 3 introduces the setup for the numerical experiments, section 4 presents the seasonal cycles of the KE energetics in both GS regions based on the reference simulation, and sections 5–7 examine the influences of seasonal surface forcing and energy advection on the seasonality of KE energetics. Finally, conclusions are summarized in section 8.

2. Analysis framework for MKE and EKE

We present definitions of KE for monthly mean and monthly varying flows in the GS region. The corresponding energy densities ($J\,m^{-3}$) are given by

$$\mathrm{MKE} = E_{k0} = \frac{1}{2}\rho_0(\overline{u}^2 + \overline{v}^2), \quad \text{and} \tag{1}$$

$$\mathrm{EKE} = \overline{E'_k} = \frac{1}{2}\rho_0\overline{(u'^2 + v'^2)}, \tag{2}$$

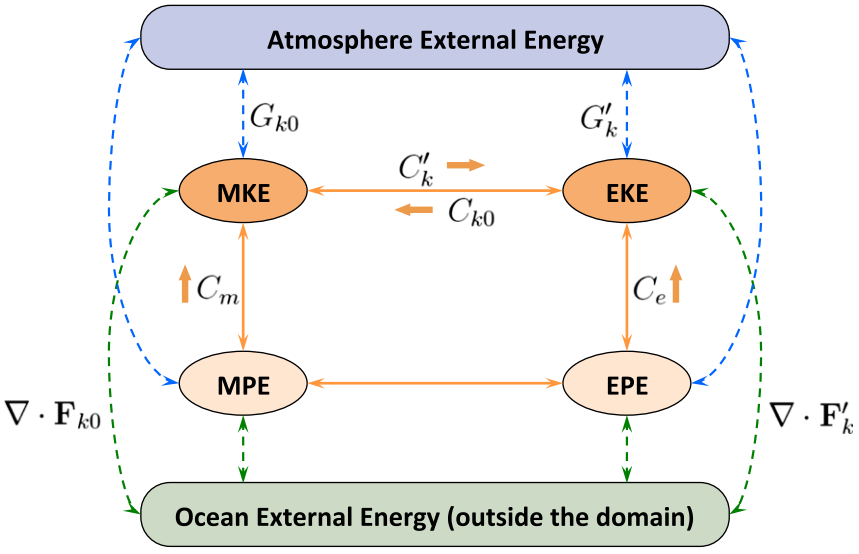

FIG. 1. Energy exchange of KE components (dark orange ovals) with APE components (light orange ovals) within a fixed ocean domain, and with external ocean and atmosphere energy (green and blue boxes, respectively). Solid arrows illustrate the energy conversion within the ocean domain, while dashed arrows indicate the energy transferring into or out of the local ocean domain. The energy exchange terms related to MKE and EKE are labeled in this diagram and defined in Eqs. (3).

where u and v are the horizontal velocity components, and $\overline{(\cdot)}$ and $(\cdot)'$ represent the monthly mean and deviation of a variable, respectively. The term $\rho_0 = 1000\,\mathrm{kg\,m^{-3}}$ is the constant reference density.

This definition is different from those in previous studies, where EKE has been estimated with respect to different time-mean basis, such as the climatological mean (Qiu 1999; Zhai et al. 2008; Scharffenberg and Stammer 2010) and the bandpass running mean with a window size of 3 months (Brachet et al. 2004), 120 days (Jouanno et al. 2012), or 300 days (Jia and Wu 2011). In our definition, MKE represents the kinetic energy of features that persist longer than one month. Therefore, MKE includes contributions from not only the GS mean currents but also the long-lived mesoscale features like stationary meanders or fixed recirculations. On the other hand, EKE measures the kinetic energy of high-frequency variability (with periods shorter than a month), and thus eliminates the low-frequency (seasonal and interannual) variability of the flow.

In the following sections, we use numerical simulations to evaluate the seasonal cycles of the KE components as defined above and their interactions with other components of the energy cycle as defined in Kang and Curchitser (2015). Figure 1 illustrates the energy exchange of MKE and EKE with APE components within a fixed ocean domain and with external ocean and atmosphere energy. The mean available potential energy (MPE) and eddy available potential energy (EPE) represent the APE densities of time-mean and time-varying flows, respectively. Their definitions are presented in Eqs. (A10)–(A11). A complete description of the energy exchange diagram is presented in Fig. 1 of Kang and Curchitser (2015). In this paper we label only the energy exchange terms related to the MKE and EKE, which we also present as follows for ease of reference:

$$
\begin{aligned}
\mathrm{MKE} \rightarrow \mathrm{EKE}(C'_k) &= -\rho_0(\overline{u'\mathbf{u}'} \cdot \nabla\overline{u} + \overline{v'\mathbf{u}'} \cdot \nabla\overline{v}),\\
\mathrm{EPE} \rightarrow \mathrm{EKE}(C_e) &= -g\overline{\rho'_a w'},\\
\mathrm{EKE} \rightarrow \mathrm{MKE}(C_{k0}) &= -\rho_0[\overline{u}\nabla \cdot (\overline{\mathbf{u}'u'}) + \overline{v}\nabla \cdot (\overline{\mathbf{u}'v'})],\\
\mathrm{MPE} \rightarrow \mathrm{MKE}(C_m) &= -g\overline{\rho_a}\,\overline{w},\\
G_{k0} &= \overline{u}\overline{\mathscr{F}_u} + \overline{v}\overline{\mathscr{F}_v},\\
G'_k &= \overline{u'\mathscr{F}'_u} + \overline{v\mathscr{F}'_v},\\
\nabla \cdot \mathbf{F}_{k0} &= \nabla \cdot (\overline{\mathbf{u}}E_{k0} + \overline{\mathbf{u}}\,\overline{p_a}),\\
\nabla \cdot \mathbf{F}'_k &= \nabla \cdot (\overline{\mathbf{u}E'_k} + \overline{\mathbf{u}'p'_a}),
\end{aligned}
\tag{3}
$$

where $\mathbf{u} = (u, v, w)$ is the velocity vector, ρ_a is the perturbation density, and p_a is the related perturbation pressure. Variables $\mathscr{F}_u$ and $\mathscr{F}_v$ are the surface wind stress in u and v directions, respectively. Energy conversion terms C'_k (MKE → EKE) and C_e (EPE → EKE) represent the EKE production due to barotropic and baroclinic instabilities of the flow, respectively. Terms C_m (MPE → MKE) and C_{k0} (EKE → MKE)

represent the acceleration of the mean flow through mean buoyancy flux and the work of Reynolds stresses between mean and perturbed flows. Variables G_{k0} and G'_k denote the generation of MKE and EKE by the surface wind work, respectively; and $\nabla \cdot \mathbf{F}_{k0}$ and $\nabla \cdot \mathbf{F}'_k$ represent the energy exchange of local KE components with external ocean domain through advection. In the appendix, we present a summary of the energy analysis framework used in this study, including the full set of energy equations for the time-mean and time-varying flows, as well as the definitions of terms not provided here.

3. Numerical experiments

We perform a set of three numerical simulations with different ocean surface forcing, as described in Table 1. The numerical ocean model used is the Regional Ocean Modeling System (ROMS) (Shchepetkin and McWilliams 2003, 2005), which solves the incompressible, hydrostatic primitive equations with a nonlinear free surface. The simulation domain covers the path of the Gulf Stream in the northwest Atlantic (Fig. 2). The model grid has a horizontal spacing of 7 km and 40 vertical terrain-following levels stretched toward the surface so as to resolve the surface boundary layers. The initial and oceanic boundary forcing are derived from the reanalysis data of the Simple Ocean Data Assimilation (SODA v2.1.6) (Carton and Giese 2008). The surface forcing is extracted from the Co-ordinated Ocean-Ice Reference Experiments (CORE v2) datasets (Large and Yeager 2009).

TABLE 1. Forcing setup of the numerical experiments.

Expt	Surface wind forcing	Surface buoyancy forcing
1	CORE v2	CORE v2
2	CORE v2	CORE v2 climatological
3	CORE v2 climatological	CORE v2

In Table 1, experiment 1 is the reference simulation, the setup of which is the same as that described in more detail in Kang and Curchitser (2013, 2015) except for the length of simulation. Experiment 1 is forced with the original surface wind and buoyancy forcing from the CORE v2 datasets. Experiment 2 is forced with climatological surface buoyancy flux, while experiment 3 is

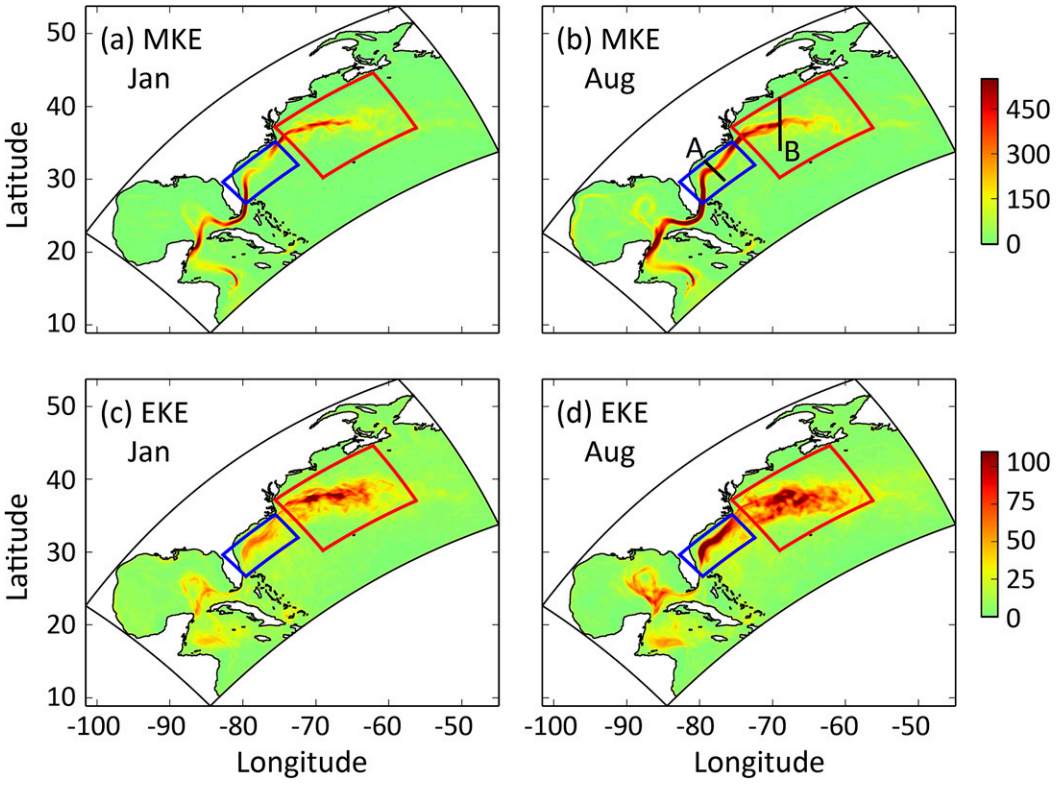

FIG. 2. Surface (a),(b) MKE and (c),(d) EKE densities (J m^{-3}) of (a),(c) January and (b),(d) August based on the reference experiment (experiment 1). The large black box outlines the entire simulation domain. The small blue and red boxes represent the GS along-coast and off-coast subdomains, respectively. The two labeled black lines in (b) indicate the two cross sections that are examined in Figs. 9–10.

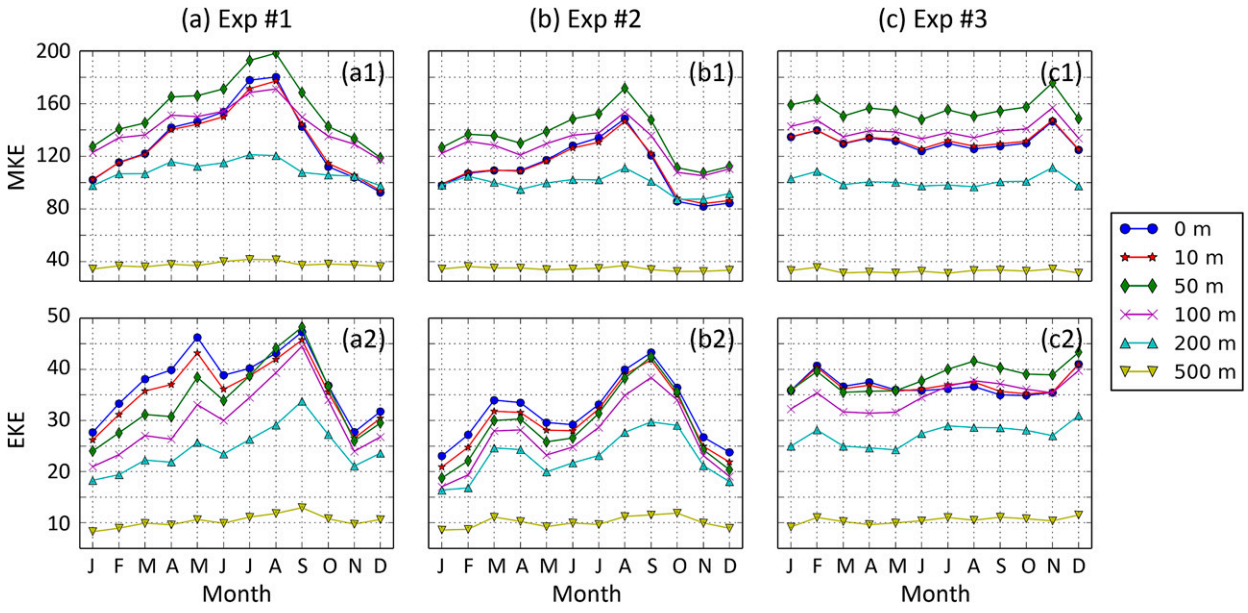

FIG. 3. Seasonal cycles of the area-mean (a1)–(c1) MKE and (a2)–(c2) EKE densities (J m^{-3}) for the GS along-coast region at six upper ocean depths. Results in columns (a)–(c) are based on the simulation results of experiments 1–3, respectively.

forced with climatological surface winds. Both climatological values are computed from the CORE v2 data. All these simulations start from the same initial conditions in 1958 and run for 10 years.

Based on the energy analysis framework presented in section 2, we use the model output to evaluate the oceanic MKE and EKE as well as their interaction terms with other local and external energy components. In the following sections, we examine the seasonal variability of the KE energetics in the GS region and investigate their connection to the seasonal cycles of the surface wind and buoyancy forcing.

4. Seasonal variability of MKE and EKE

In this section, we examine the seasonal variability of KE components and their interactions with other energy components in the GS region based on the reference simulation with realistic surface forcing.

Figure 2 illustrates the horizontal distribution of the winter (January) and summer (August) surface MKE and EKE densities averaged over the entire simulation period of the reference experiment. The spatial pattern of each energy component is similar in both seasons. However, both MKE and EKE densities are higher in summer months. The blue and red boxes in each plot outline two GS subdomains upstream and downstream of Cape Hatteras, respectively. Hereinafter, these two domains are referred to as the GS along-coast and off-coast domains, respectively. In this study, we focus on examining the seasonal cycle of the KE energetics in these two regions.

Figures 3–4 demonstrate the mean seasonal cycles of the upper ocean MKE and EKE densities averaged over the two subdomains, respectively. Column A presents the results of the reference simulation. In the along-coast region, the area-mean upper ocean MKE density has a clear seasonal cycle, with the maximum/minimum in the summer/winter seasons (Fig. 3a1). The August maximum is almost twice as intense as the December minimum for the upper 100 m. The surface EKE density in this region has two comparable peaks in May and September, respectively (Fig. 3a2). The September peak is consistently strong throughout the upper oceans, while the May peak decays by nearly one-half from the surface to 200-m depth.

In the off-coast region, the area-mean MKE density has a weak seasonal cycle that peaks in the summer season (Fig. 4a1). The surface EKE density has a dominant peak in May and a secondary peak in September (Fig. 4a2). The May peak decays quickly downward and disappears at 100-m depth, while the September peak remains in the upper oceans and becomes the sole peak at depths deeper than 100 m.

We note that in the along-coast region, MKE is nearly 4 times as intense as EKE and its seasonal variability is more significant than that of EKE. While in the off-coast region, EKE is slightly weaker than MKE, but its seasonal variability has a larger amplitude. Based on the definitions of MKE and EKE in section 2, our results

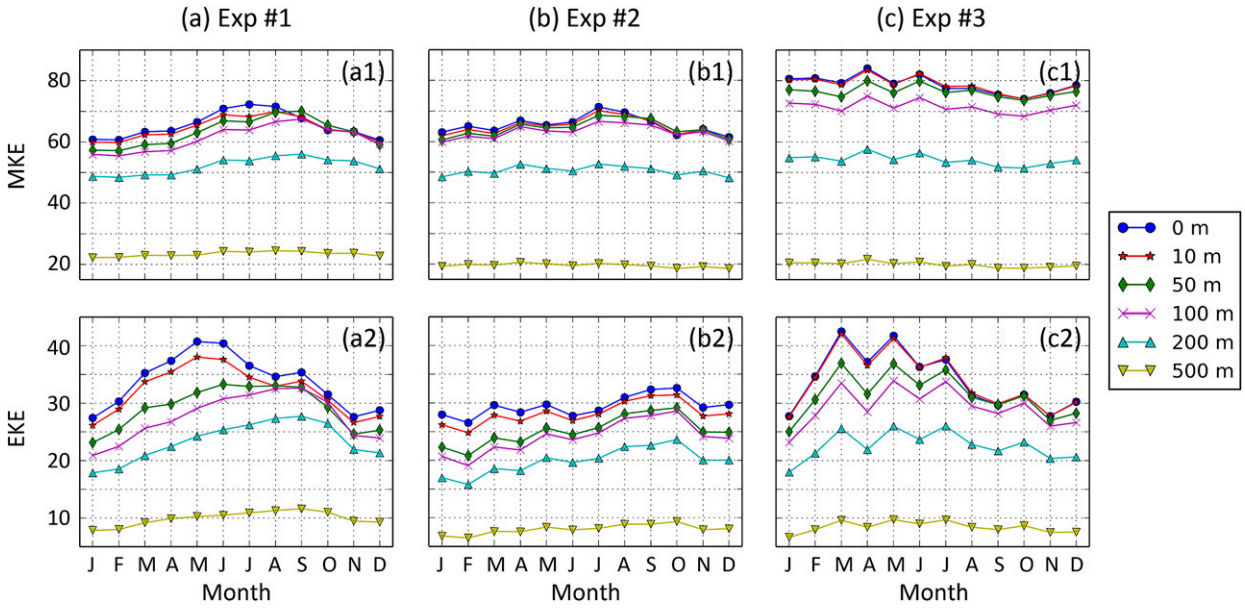

FIG. 4. As in Fig. 3, but for the GS off-coast region.

indicate that long-lived features play a more significant role in shaping the seasonal cycle of KE in the GS along-coast region, while high-frequency features are more important in the off-coast region.

We further examine the seasonal cycles of the area-mean upper ocean energy conversion rates for the two subdomains (Figs. 5–6). Results of the reference experiment are depicted in column A. In the along-coast region, the barotropic conversion rate (MKE → EKE) has a sharp positive peak in August–September (Fig. 5a1). This indicates that a strong EKE production due to horizontal shear instability takes place during this season, which is related to the September peak of EKE in this region. On the other hand, the baroclinic conversion rate (EPE → EKE) has a strong peak during January–March for the upper 100 m (Fig. 5a2). At depths deeper than 200 m, the seasonal cycle of this conversion reverses to peak in summer. This indicates that in late winter and early spring, the flow is the most baroclinically unstable in the upper 100 m of the water column. The May peak of upper ocean EKE lags this peak of baroclinic instability by 2–3 months. A similar correlation between the surface EKE and the baroclinic instability was also observed in the North Pacific (Qiu 1999) and the southeast Indian Ocean (Jia and Wu 2011). In those studies, the authors employed a theoretical model to show that the lag of a couple of months is the length of time for unstable waves to fully grow in the respective regions. These results suggest that the large amount of upper ocean eddy available potential energy is released in late winter/early spring through baroclinic instability and is gradually converted into EKE in late spring. We will further discuss the mechanism of barotropic and baroclinic instability in the following two sections. The energy conversions to MKE from EKE and MPE are mostly negative in the upper 500 m and have negative peaks in summer (Figs. 5a3–a4). This shows that the seasonal cycle of MKE in this region has no direct connection to the local energy conversion, which indicates that MKE might obtain energy from external energy sources and then convert it to other local energy components in the along-coast region.

In the off-coast region, there is an intense negative barotropic conversion (MKE → EKE) in late spring and early summer, which indicates that the KE of the high-frequency varying flows is converted back to the low-frequency one during this season (Fig. 6a1). The seasonal cycle of EKE has no direct connection to the barotropic instability in this region, unlike that in the along-coast region. The seasonal cycle of the baroclinic conversion (EPE → EKE) in this region resembles the one in the along-coast region. It has a strong and wide peak during late winter and early spring; however, the peak penetrates deeper to 200-m depth (Fig. 6a2). In this region, MKE extracts energy from the EKE field with a peak in late spring and early summer throughout the upper 500 m (Fig. 6a3). The energy conversion from MPE to MKE is positive in the upper 100 m with a peak in winter, while it is negative at depths deeper than 200 m with a negative peak in summer (Fig. 6a4). Neither of these local conversions has a direct connection to the seasonal cycle of

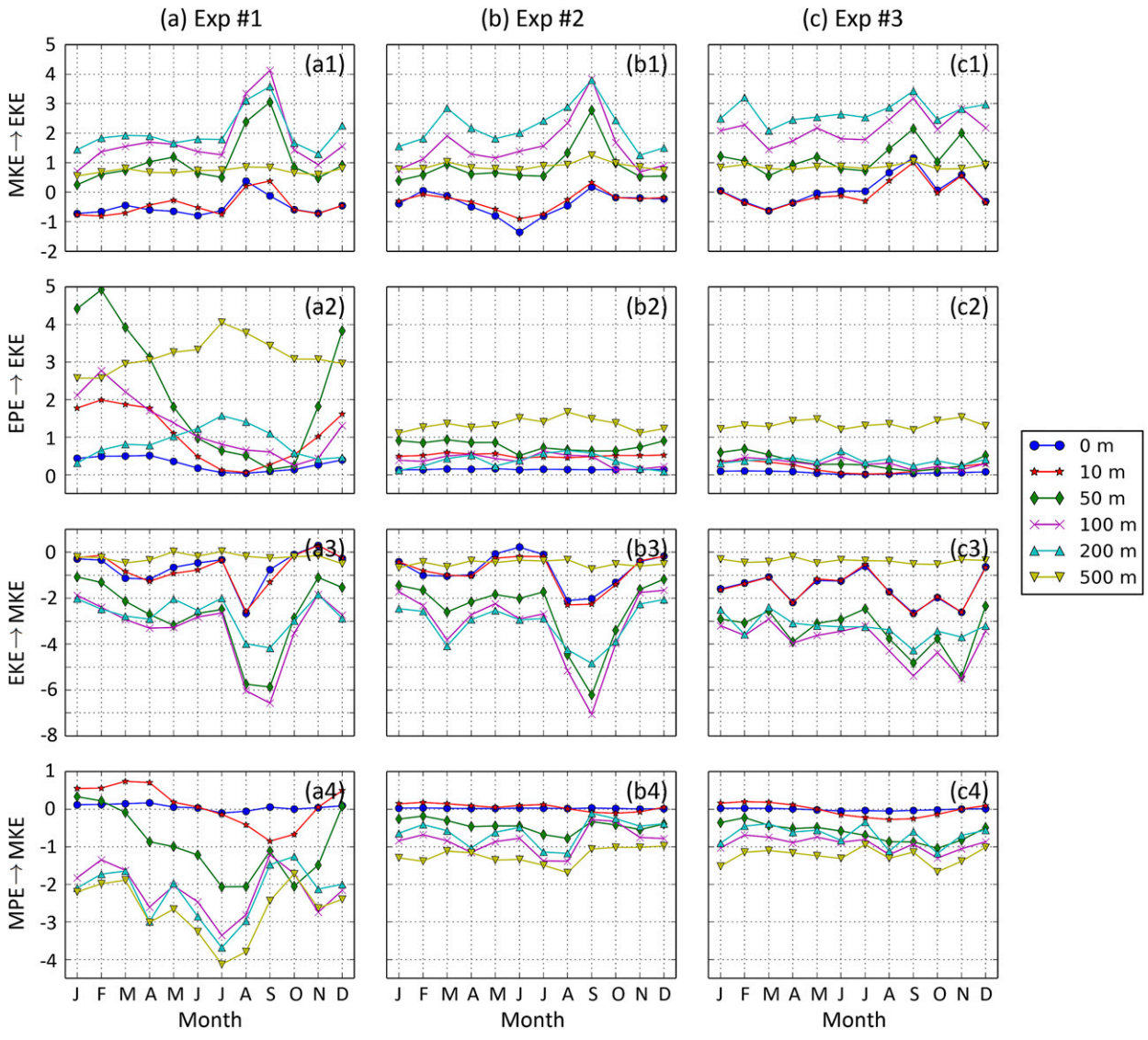

FIG. 5. Seasonal cycles of the area-mean energy conversion rates (10^{-5} W m^{-3}) for the GS along-coast region at six upper ocean depths. Results in columns (a)–(c) are based on the simulation results of experiments 1–3, respectively.

MKE in this region, indicating an external influence on the off-coast MKE seasonality.

5. Influence of surface wind forcing

In this section, we compare the results of the reference experiment to those of experiments 2–3 in order to examine the effect of seasonal surface wind forcing on the seasonal variability of KE energetics in the GS region.

In experiment 2, the seasonal variability of the surface buoyancy flux is removed while maintaining the seasonal surface winds (column B of Figs. 3–6). In the along-coast region, both KE energy components show clear seasonal cycles. The seasonal cycle of the MKE density is similar to that of the reference experiment although the August peak is slightly weaker (Fig. 3b1). The EKE density has a main peak in September and a secondary peak in March throughout the upper 500 m of the water column (Fig. 3b2). Compared to the EKE cycle of experiment 1, the September peak is slightly weaker, while the spring peak decreases significantly and shifts two months ahead. In this region, the barotropic conversion rate (MKE → EKE) has a main peak in September and a secondary peak in March, which correspond to the two peaks of the EKE cycle (Fig. 5b1). The seasonal cycle of EKE → MKE conversion resembles that of experiment 1 except for a weak negative

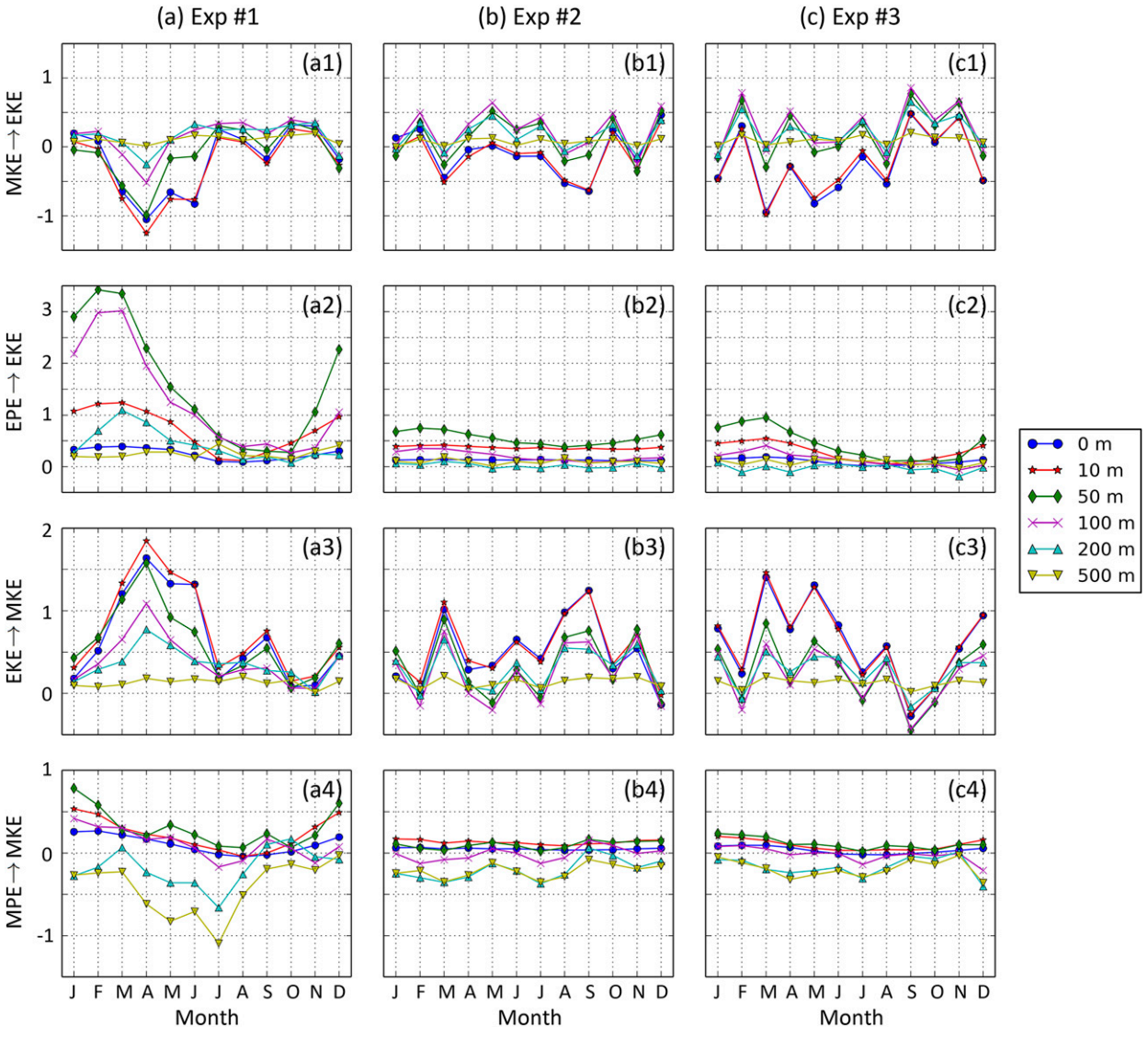

FIG. 6. As in Fig. 5, but for the GS off-coast region.

peak in March (Fig. 5b3). The conversion rates of EPE → EKE and MPE → MKE do not show clear seasonal cycles (Figs. 5b2,b4). In the off-coast region, the MKE density retains its seasonal cycle that peaks in summer although it is even less significant than that in experiment 1 (Fig. 4b1). For the EKE cycle, the surface main peak in late spring disappears, while the weak peak in late summer remains (Fig. 4b2). Not all energy conversion rates show a clear seasonal cycle (Figs. 6b1–b4).

We next examine the results of experiment 3, where the seasonal variability of the surface wind forcing is removed while retaining the seasonal variability of the surface buoyancy flux (column C of Figs. 3–6). In the along-coast region, there are no clear seasonal cycles for MKE and EKE (Figs. 3c1,c2), nor for the barotropic and baroclinic conversions (Figs. 5c1,c2). In the off-coast region, the MKE density does not show a clear seasonal cycle (Fig. 4c1); however, the EKE density has a strong peak in spring throughout the upper water column (Fig. 4c2). Compared to the EKE cycle of experiment 1, the September peak disappears, while the spring peak remains and shifts two month ahead. Energy conversion from EKE to MKE is observed in the spring season (Figs. 6c1,c3). The baroclinic conversion rate has a peak in early spring although it is much weaker than in experiment 1 (Fig. 6c2).

The above comparisons suggest that the seasonal variability of wind forcing plays a crucial role in determining the seasonal cycles of MKE and EKE, as well as their conversion in the GS along-coast region.

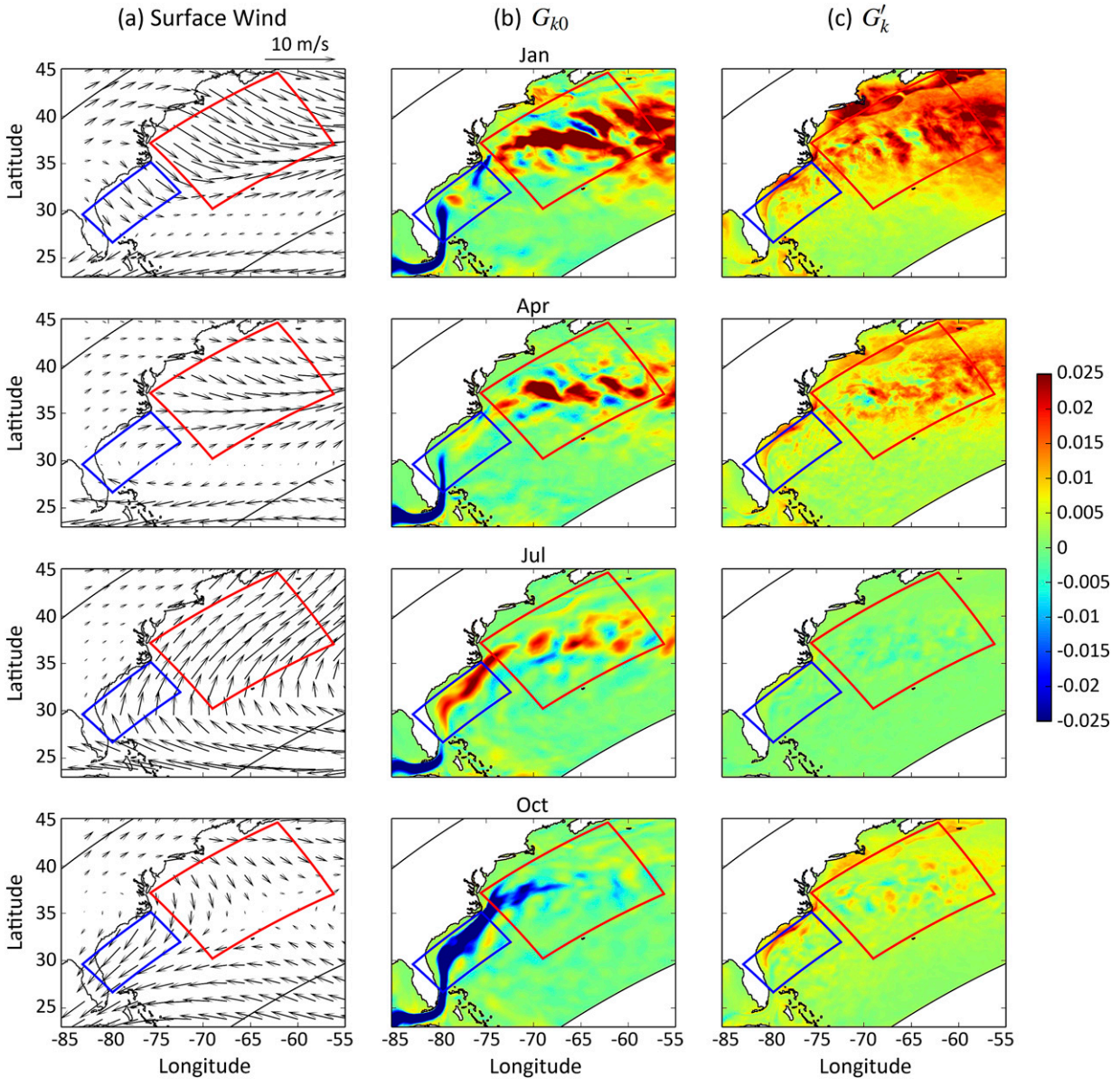

FIG. 7. Seasonal cycles of (a) surface wind (m s^{-1}), (b) G_{k0} (W m^{-2}), and (c) G'_k (W m^{-2}) in the GS region. The surface wind is based on the climatological CORE v2 data, while G_{k0} and G'_k are based on the simulation results of the reference experiment (experiment 1).

Without realistic seasonally varying wind forcing, no clear seasonal cycles of MKE and EKE are maintained in this region. In the GS off-coast region, the MKE cycle and the late summer peak of EKE seem to be related to the seasonal surface wind forcing. However, the spring peak of EKE is maintained even without the seasonal wind cycle.

Now we investigate the seasonal variability of the wind forcing and its direct and indirect local influences on the seasonal variability of MKE and EKE in both regions. Figure 7 illustrates the seasonal cycle of the surface wind as well as the cycles of wind work to the MKE and EKE fields based on experiment 1. In the along-coast region, the summer surface wind is the strongest and blows in the same direction as the GS flows (Fig. 7a, July). Accordingly, the along-coast MKE generation by surface wind work (G_{k0}) is the largest in summer (Fig. 7b, July). Figure 8a compares the seasonal cycles of the area-mean G_{k0} for the three experiments in this region. A positive peak in summer can be clearly seen for experiments 1–2, while no seasonal cycle remains for experiment 3, in which the

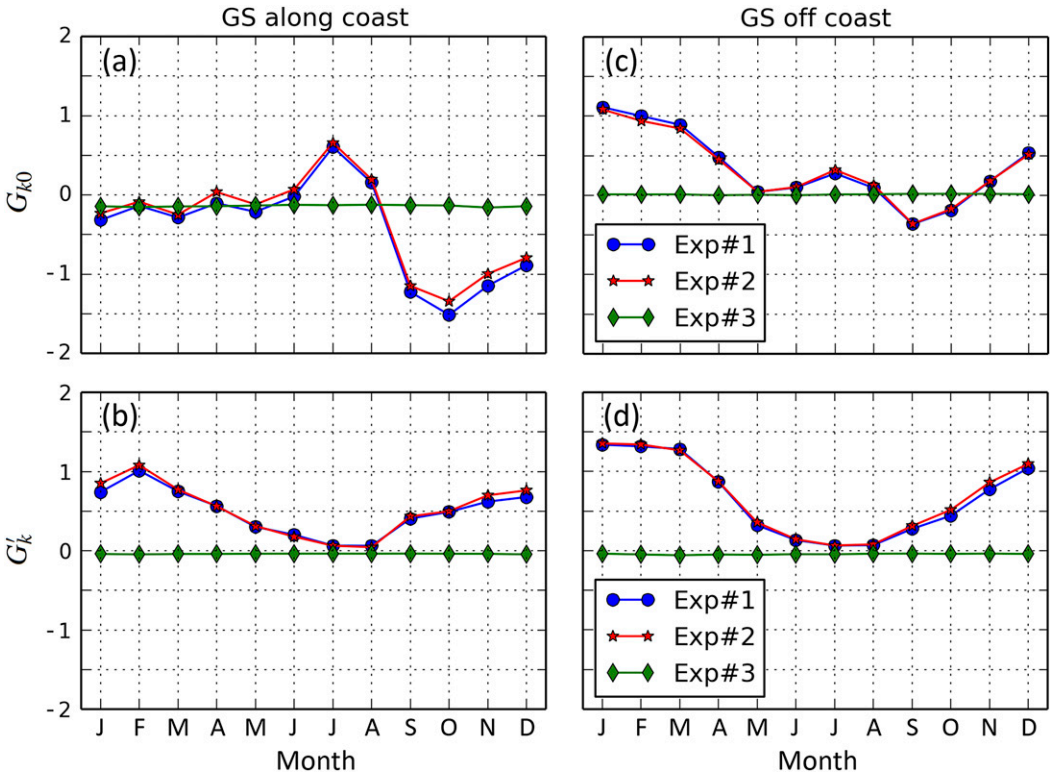

FIG. 8. Seasonal cycles of the area-mean G_{k0} and G'_k (10^{-2} W m^{-2}) for the GS (left) along-coast and (right) off-coast regions based on the simulation results of experiments 1–3.

seasonal variability of the wind forcing is removed. These results are consistent with the features of MKE variability observed in this region (Figs. 3a1,b1,c1). On the other hand, the along-coast EKE generation by surface wind work (G'_k) has a seasonal cycle that peaks in late winter and early spring (Figs. 7c and 8b). The enhanced EKE generation by wind in this season might contribute to the spring peak of EKE in experiments 1–2 (Figs. 3a2,b2); however, it has no direct connection to the September peak of EKE in the along-coast region.

Although the local wind generation has no direct influence on the late summer peak of EKE in the along-coast region, the local wind can indirectly affect the EKE cycle by changing the mean flow instability. Figures 9–10 compare the seasonal variations of the mean currents' vertical profile across sections A and B (indicated in Fig. 2b), respectively, for the three experiments. With the realistic surface wind forcing (experiments 1–2), the mean flow strength and its horizontal shear in the along-coast region both peak in the summer season (Figs. 9a,b). This indicates that the along-coast mean flow is the most barotropically unstable in summer, and therefore generates the largest amount of EKE through barotropic instability in this season. When the seasonal cycle of the surface wind forcing is removed (experiment 3), no clear seasonal variability is evident in the mean flow strength and its horizontal shear (Fig. 9c). These results and the seasonal variability of the MKE → EKE conversion (Figs. 5a1,b1,c1) both suggest that in the along-coast region the September peak of EKE is mainly due to the seasonally varying barotropic instability, and therefore is indirectly connected to the seasonal variability of wind forcing.

In the off-coast region, the MKE and EKE generations by local surface wind (G_{k0} and G'_k) both peak in winter (Figs. 7b,c and 8c,d). This seasonal variability has no direct relation to the seasonal cycles of MKE and EKE in this region. The horizontal shear of the off-coast mean flow does not exhibit a clear seasonal cycle in the three experiments (Fig. 10), indicating that barotropic instability is not a major mechanism governing the seasonal cycle of EKE in this region. These results show that neither the local wind generation of energy, nor the local flow barotropic instability can explain the MKE cycle and the September peak of EKE cycle in the off-coast region. One possibility is

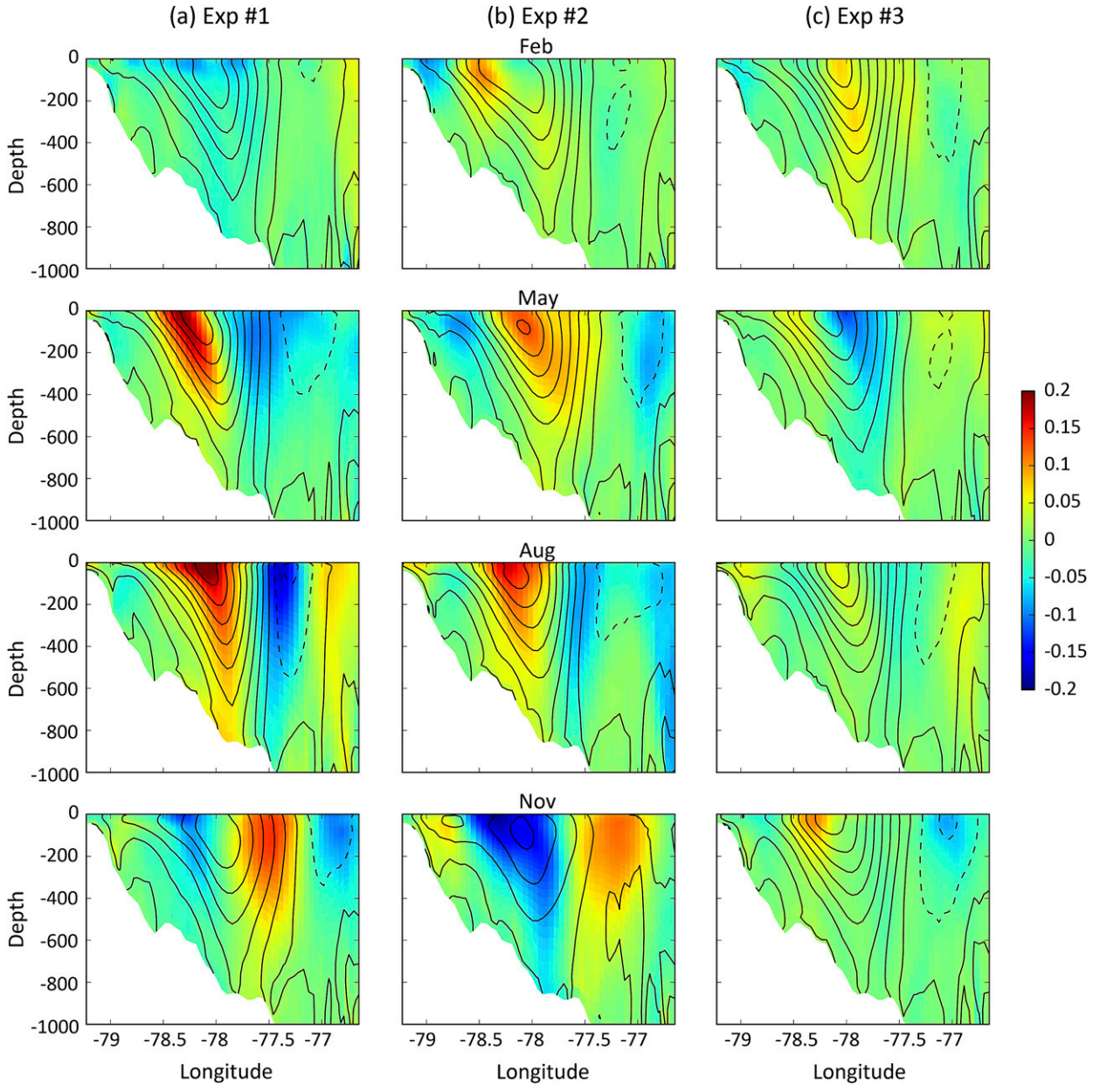

FIG. 9. Seasonal cycles of the vertical structure of monthly mean currents (contours, m s^{-1}) and anomalies (colors, m s^{-1}) across the section within the GS along-coast region (indicated by A in Fig. 2b). The contour interval is 0.1, and the solid and dashed contours indicate positive and negative values, respectively. Results in columns (a)–(c) are based on the simulation results of experiments 1–3, respectively.

that this variability comes from the remote region through energy advection. We will further explore this in section 7.

6. Influence of surface buoyancy forcing

As in section 5, we compare the results of experiments 1–3 to examine the effect of seasonal surface buoyancy forcing on the seasonal variability of KE energetics in the GS region.

When the seasonal cycle of the surface buoyancy forcing is removed while the seasonality of the wind forcing is retained (experiment 2), the most affected feature in both analysis regions is the spring peak of EKE (Figs. 3b2–4b2) and the baroclinic conversion from EPE to EKE (Figs. 5b2–6b2).

When the realistic seasonal surface buoyancy forcing is maintained while the seasonal cycle of the wind forcing is removed (experiment 3), there is no clear seasonal cycle for the along-coast MKE or EKE, or for the off-coast

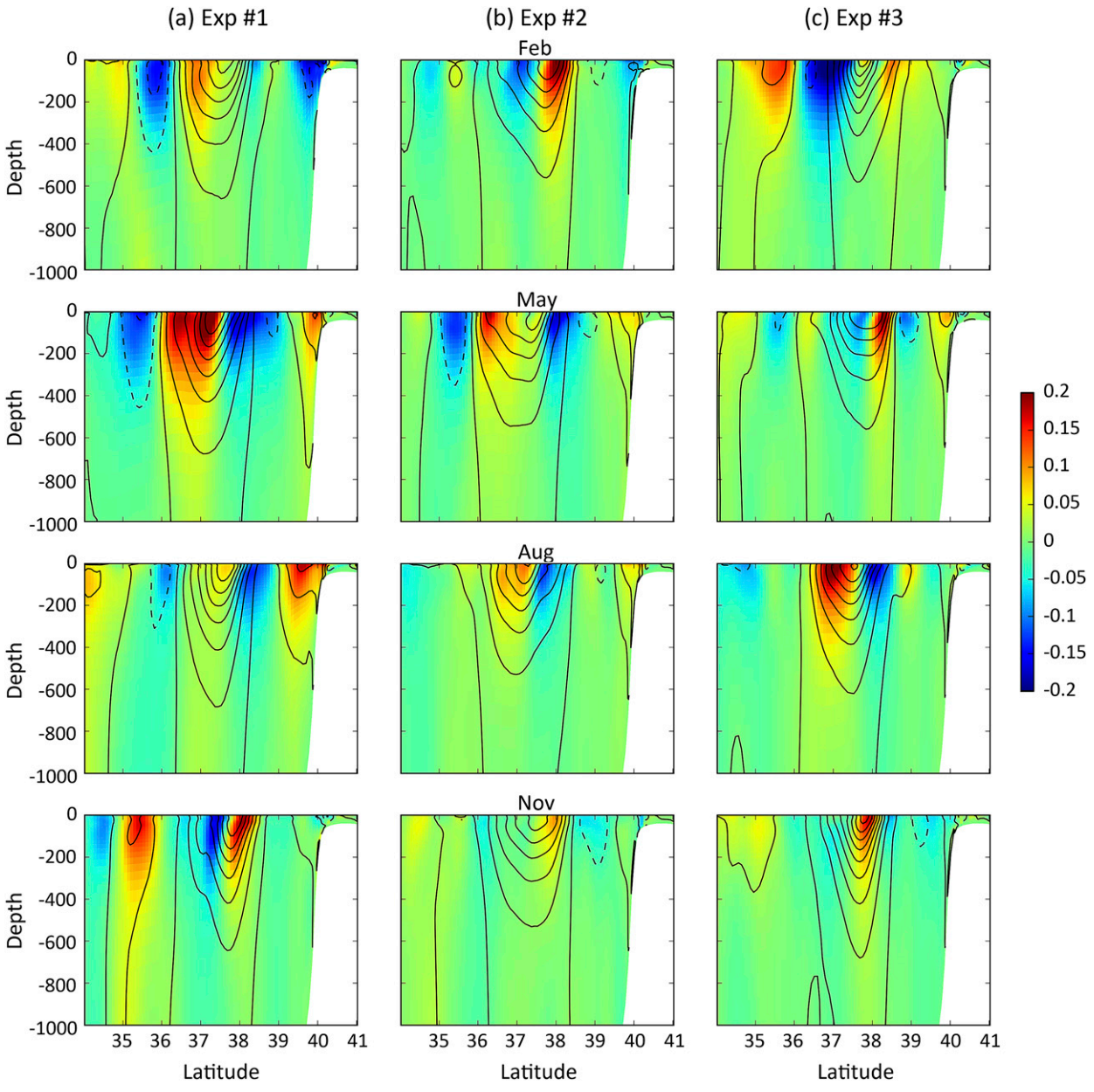

FIG. 10. As in Fig. 9, but for the section within the GS off-coast region (indicated by B in Fig. 2b).

MKE. For the off-coast EKE cycle, the late summer peak disappears while the spring peak remains strong.

These comparisons suggest that the spring peak of upper ocean EKE is closely related to the seasonal variability of the surface buoyancy forcing. This relation is more significant in the GS off-coast region.

Based on the eddy and mean flow energy equations presented in Kang and Curchitser (2015), the surface buoyancy forcing has no direct contributions to the generation of MKE and EKE. However, its seasonal variability can influence the EKE cycle by changing the baroclinic instability of the flow. Figures 11–12 compare the seasonal variations of the vertical thermal structure across sections A and B, respectively, for the three experiments. In experiment 1 (Figs. 11a–12a), the upper ocean is well stratified in summer/early autumn for both regions. The isotherms start to tilt during late autumn and reach their maximum steepness in late winter/early spring, indicating that the flow is the most baroclinically unstable during this season. In late spring, the isotherms start to flatten and then, in summer, form a shallow and flat thermocline. This annual cycle of the vertical thermal

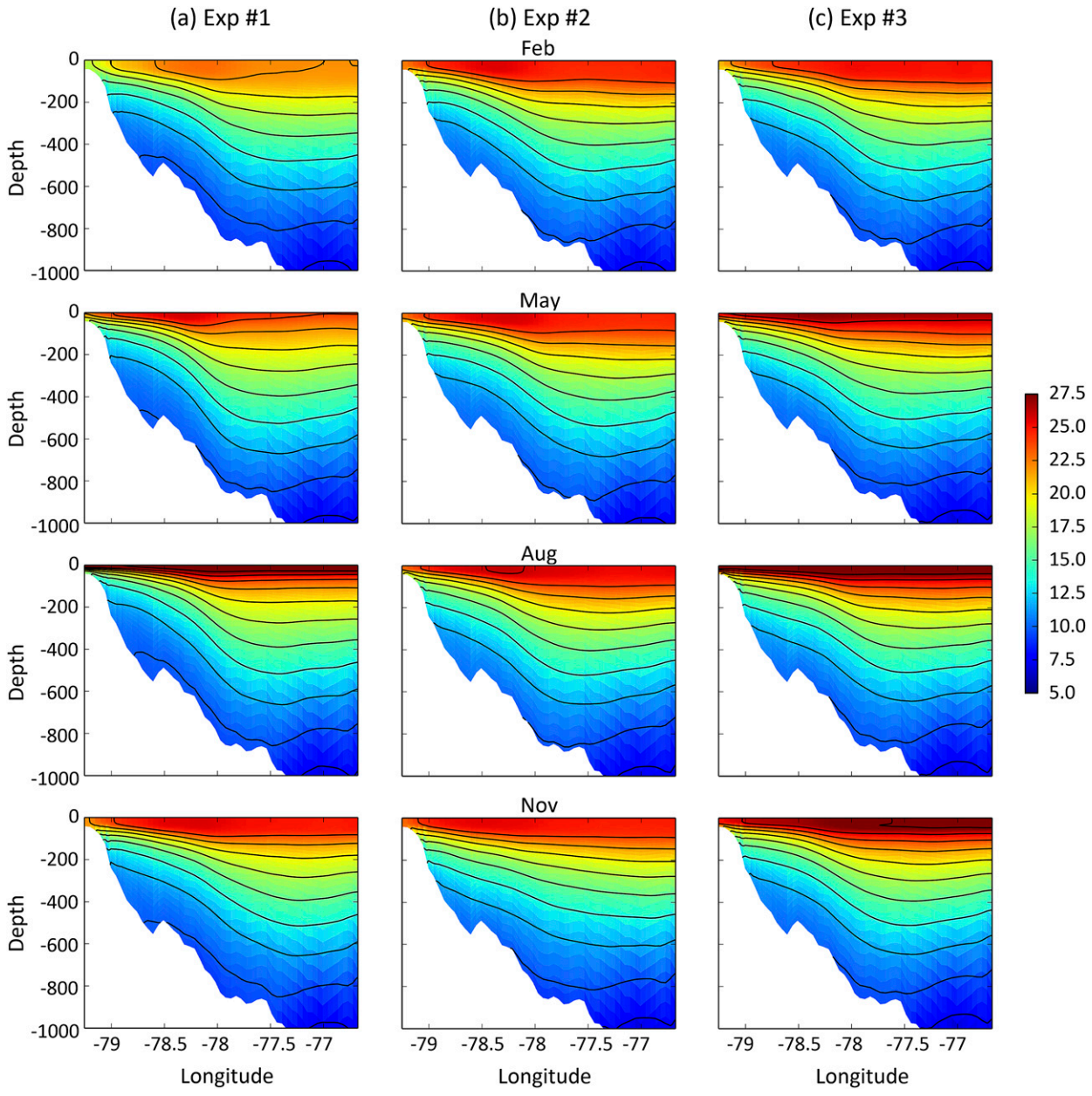

FIG. 11. Seasonal cycles of the vertical thermal structure (°C) across the section within the GS along-coast region (indicated by A in Fig. 2b). Results in columns (a)–(c) are based on the simulation results of experiments 1–3, respectively.

structure was also observed across the GS along both 60° and 65°W based on the *World Ocean Atlas* (Zhai et al. 2008) and in an ocean model simulation (Kang and Curchitser 2013), respectively. This feature, along with the seasonal cycle of EPE → EKE (Figs. 5a2–6a2), suggests that the large amount of EPE built up in late winter/early spring is released and converted into EKE in late spring via baroclinic instability. These results connect the spring peak of the upper ocean EKE to the baroclinic instability of the flow in the GS region.

The baroclinic instability is affected by the variability of both the wind and buoyancy forcing. When the seasonal variability of either surface forcing is removed (experiment 2 or 3), the build-up cycle of the seasonal thermocline becomes less significant (Figs. 11b,c–12b,c) and thus the baroclinic instability is substantially reduced (Figs. 5b2,c2–6b2,c2). Figure 13 compares the seasonal cycles of the area-mean mixed layer depth for the three experiments in both regions. It confirms that the seasonally varying wind and buoyancy forcing

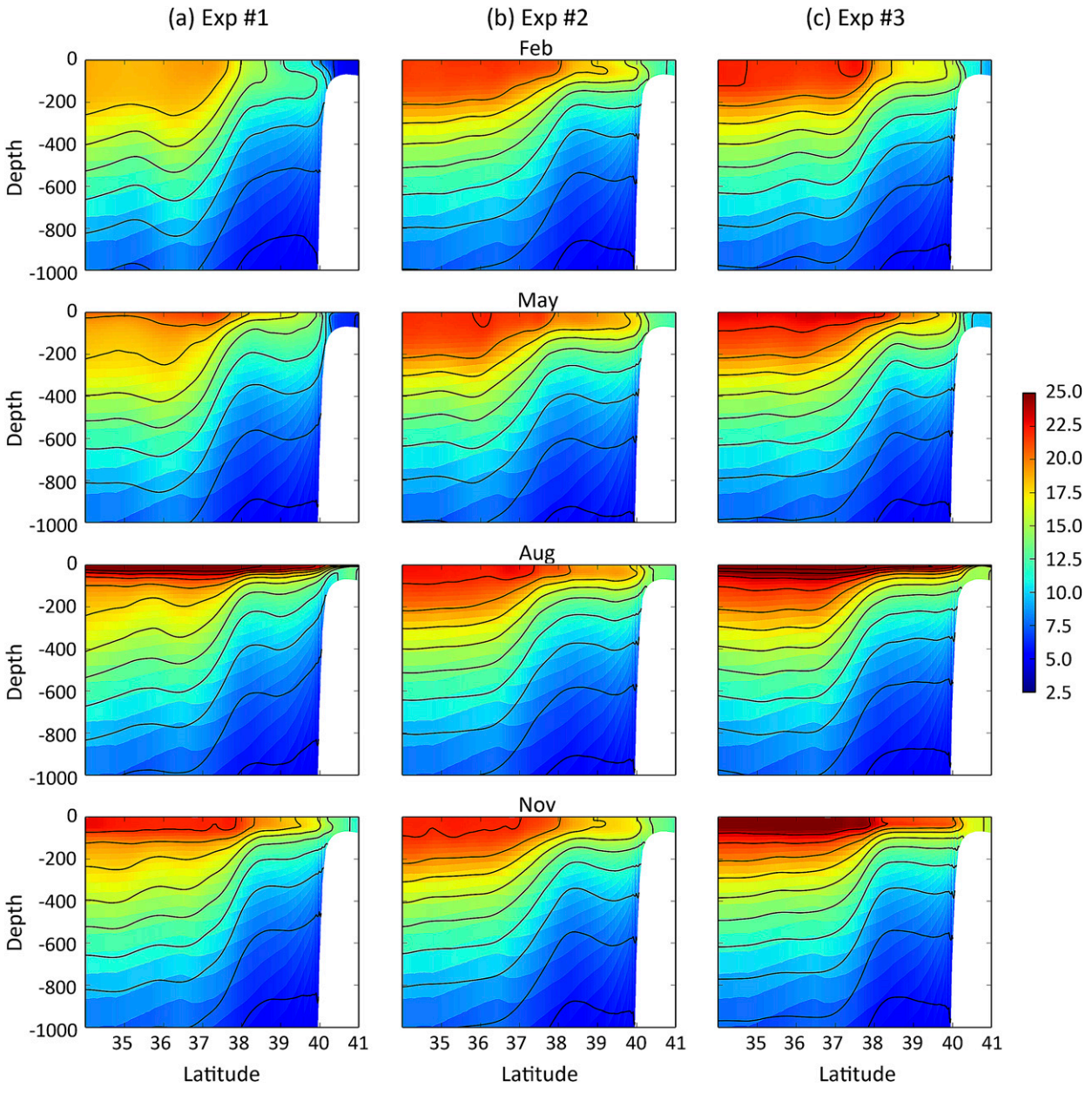

FIG. 12. As in Fig. 11, but for the section within the GS off-coast region (indicated by B in Fig. 2b).

both affect the seasonal cycle of baroclinic instability. In the off-coast region, the buoyancy forcing plays a more important role compared to that in the along-coast region (Fig. 13). In experiment 1, the spring peak of surface EKE is much stronger than the September peak in the off-coast region (Fig. 4a2), while it has comparable strength to the September peak in the along-coast region (Fig. 3a2). In experiment 3, which is only forced by the realistic seasonal buoyancy flux, the spring peak of EKE remains strong in the off-coast region (Fig. 4c2), while it disappears in the along-coast region (Fig. 3c2).

7. Influence of energy advection

In sections 5–6, we examined the effect of seasonal atmospheric forcing on the seasonal variability of KE dynamics in the GS region. In this section, we further explore the influence of the seasonally varying ocean environment external to our focus region.

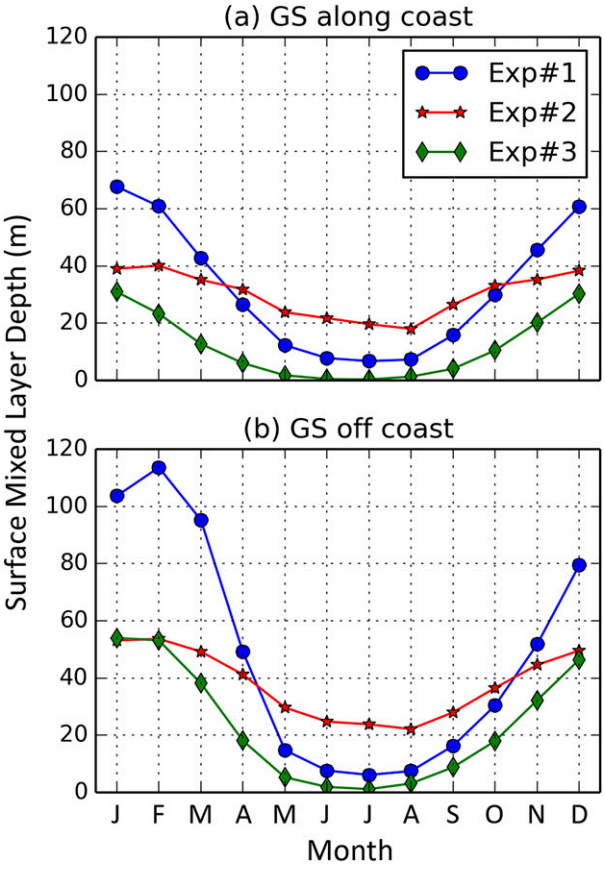

FIG. 13. Seasonal cycles of the area-mean surface mixed layer depth for the GS (a) along-coast and (b) off-coast regions based on the simulation results of experiments 1–3.

Our previous analysis has shown that the seasonal wind forcing plays an important role in determining the September peak of EKE in the GS along-coast region by influencing the seasonality of the flow barotropic instability mechanism. On the other hand, the seasonal buoyancy forcing is closely connected to the spring peak of the upper ocean EKE in both along- and off-coast regions through the seasonality of the flow baroclinic instability mechanism. Moreover, the seasonal cycle of along-coast MKE is related to the seasonal variability resulting from direct forcing by the local wind. The seasonal cycle of MKE and the late-summer peak of EKE in the off-coast region are related to the seasonal wind forcing, which is retained in experiment 2, but omitted in experiment 3. We note that there is no evidence to connect them to the seasonal cycle of either the local energy generation by wind or to the local flow barotropic instability. We therefore consider the possible mechanism that the seasonal variability comes from the remote regions through the advection of energy.

We examine the seasonal cycles of the upper ocean energy flux divergence terms [Eqs. (3) in both GS subdomains (Figs. 14–15). The positive and negative values represent the power transferring out of and into the local domain, respectively. In the along-coast region, the divergence of MKE flux has an intense negative peak for experiments 1–2, while it has no clear seasonal cycle for experiment 3 (Figs. 14a1,b1,c1). These results indicate that the seasonal cycle of along-coast MKE is influenced by the seasonality of remote energy advection, in addition to the direct energy generation by local wind as we have seen in section 5. The divergence of EKE flux in the along-coast region is mostly positive in upper 200 m with a major positive peak in summer and a secondary peak in spring for experiment 1 (Fig. 14a2). This indicates that EKE is being advected from the along-coast region in the upper 200 m of the water column.

In the off-coast region, the divergence of MKE flux is negative throughout upper 500 m and has a negative peak in summer for experiment 1 (Fig. 15a1). The seasonal cycle becomes weaker for experiment 2 (Figs 15b1) and there is no clear seasonal cycle for experiment 3 (Fig. 15c1). These results suggest that the off-coast region is a sink of MKE and the weak seasonal variability of local MKE could come from an upstream source in the along-coast region. Finally, the divergence of EKE flux in the off-coast region is negative throughout the upper 500-m depths and has two peaks in late winter and late summer for experiment 1 (Fig. 15a2). The late summer peak remains for experiment 2 (Fig. 15b2), while it disappears for experiment 3 (Fig. 15c2). The weak late-summer peak of EKE in the off-coast region seems to be related to this wind-dependent late summer peak of EKE convergence. The above results imply that the late summer peak of EKE in the GS off-coast region is connected to the seasonality in remote signals through energy advection, which could include the eddy signals propagating downstream from the along-coast region, or the Rossby waves and mesoscale eddy signals propagating westward from the ocean interior.

8. Summary and discussion

In this study, we examined the seasonal variability of the upper ocean kinetic energy in the Gulf Stream region using high-resolution regional ocean model simulations. We performed a set of three numerical experiments varying the surface wind and buoyancy forcing in order to investigate the mechanisms governing the seasonal cycle of upper ocean KE dynamics in the GS along- and off-coast regions.

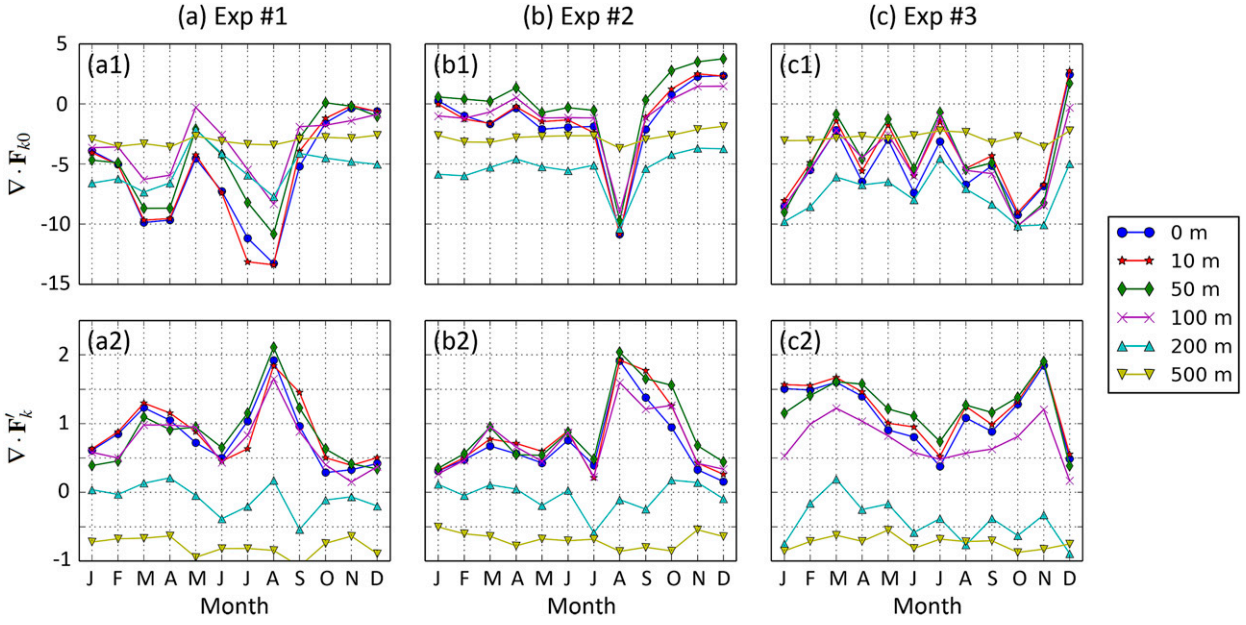

FIG. 14. Seasonal cycles of the area-mean energy flux divergences (10^{-5} W m^{-3}) for the GS along-coast region at six upper ocean depths. Results in columns (a)–(c) are based on the simulation results of experiments 1–3, respectively.

We split the ocean energy components into monthly mean and monthly varying parts. Based on the eddy and mean flow energy equations previously derived in Kang and Curchitser (2015), we evaluated the seasonal variability of the KE components (MKE and EKE) and their interactions with other energy components both within the regional ocean domain and with the energy of the external ocean and atmosphere.

In the GS along-coast region, the MKE has a significant seasonal cycle that peaks in summer, while the EKE has peaks in May and September throughout the upper 500 m of the water column. The two peaks of EKE have comparable strength at the sea surface, however, the May peak decays significantly with depth so that the September peak dominates the EKE cycle below the surface. The barotropic conversion from MKE to EKE has a

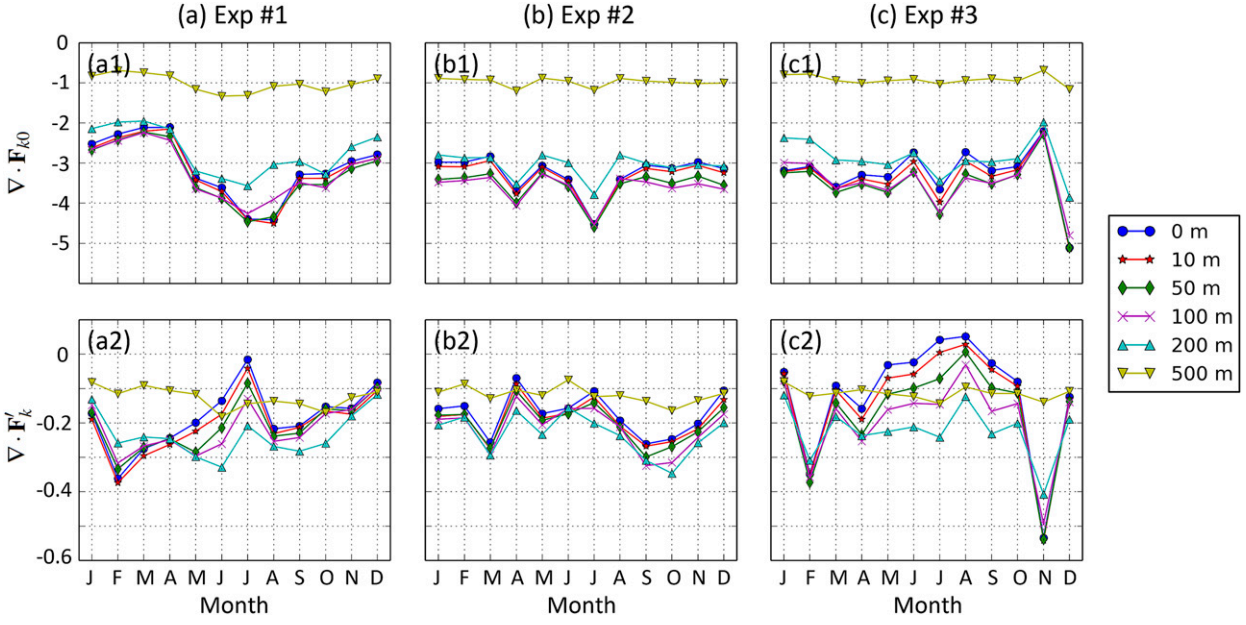

FIG. 15. As in Fig. 5, but for the GS off-coast region.

sharp and strong peak in the summer season, whereas the baroclinic conversion from EPE to EKE has a wide and strong peak in late winter and early spring.

In the GS off-coast region, the MKE has a weak seasonal cycle that peaks in summer, whereas the EKE has a dominant peak in May and a secondary peak in September near the sea surface. The May peak decays rapidly with depth and the September peak becomes the sole peak of the EKE cycle at depths greater than 100 m. The barotropic conversion has no clear seasonal cycle, while the baroclinic conversion has a wide and strong peak in late winter and early spring as in the along-coast region.

We analyzed the three numerical simulations in order to examine the influence of seasonal variability in the surface forcing on the observed seasonal cycle of KE. Our results suggest that the seasonal cycle in the local wind forcing plays a dominant role in determining the seasonality of the flow barotropic instability and consequently drives the late summer peak of EKE in the along-coast region. Conversely, it is the seasonality in the buoyancy forcing term that is the primary driver for the seasonal cycle of the baroclinic instability processes and, therefore, closely related to the late spring peak of upper ocean EKE in both our subregions. Moreover, the seasonal variability of MKE in the along-coast region is forced by the local energy generation by the wind as well as the variability advected into this region from upstream locations. Finally, the MKE cycle and the September peak of EKE in the off-coast region is related to the seasonal cycle in the wind forcing. However, we find no direct connection to the local energy generation by the wind nor to the barotropic conversion implying that such seasonal variability in the off-coast region is mainly due to advection of energy from the remote region.

In this study, we defined MKE and EKE with respect to a monthly mean reference. Therefore, the MKE includes contributions from both the GS mean currents and long-lived mesoscale features. Using our definition, EKE represents the KE of high-frequency variability and eliminates contributions from the seasonal and interannual variability of the flow. This definition is different from previously published works, which were based on different definitions of the time-mean flow such as the climatological mean (Qiu 1999; Zhai et al. 2008; Scharffenberg and Stammer 2010) and the bandpass running mean with a window size of 3 months (Brachet et al. 2004), 120 days (Jouanno et al. 2012), or 300 days (Jia and Wu 2011). Using our definition, MKE is nearly 4 times as intense as EKE and its seasonal variability is more significant than that of EKE in the along-coast region. Whereas in the off-coast region EKE is slightly weaker than MKE and its seasonal variability has a larger amplitude. These results indicate that long-lived features play a more important role in shaping the seasonal cycle of KE in the GS along-coast region, while the high-frequency features are more significant in the off-coast region. In follow-on work we will investigate features that arise from an alternative choice of frequency filtering. Furthermore, the current analysis techniques set the framework for investigating the seasonal variability of the domain-integrated energetics and ultimately observed interannual variability in the Gulf Stream region.

Acknowledgments. The authors gratefully acknowledge the support of the National Science Foundation through Awards OCE-1049088, OCE-1419584, and OCE-0961545; and the National Oceanic and Atmospheric Administration through Awards NOAA-NA-13OAR4830233 and NOAA-NA-15OAR4310133. Some of the computations were carried out at the National Center for Atmospheric Research in Boulder, Colorado. We also thank two anonymous reviewers for their valuable comments and suggestions.

APPENDIX

Energetics of the Mean Flow and Eddies

In this study, we investigate the seasonal variability of MKE and EKE in the GS region based on the energy analysis framework presented in Kang and Curchitser (2015). Here we summarize this framework for ease of reference.

The governing equations are given by

$$\frac{\partial u}{\partial t} + \mathbf{u}\cdot\nabla u - fv = -\frac{1}{\rho_0}\frac{\partial p}{\partial x} + \mathscr{F}_u + \mathscr{D}_u, \tag{A1}$$

$$\frac{\partial v}{\partial t} + \mathbf{u}\cdot\nabla v + fu = -\frac{1}{\rho_0}\frac{\partial p}{\partial y} + \mathscr{F}_v + \mathscr{D}_v, \tag{A2}$$

$$\frac{\partial p}{\partial z} = -\rho g, \tag{A3}$$

$$\frac{\partial C}{\partial t} + \mathbf{u}\cdot\nabla C = \mathscr{F}_C + \mathscr{D}_C, \quad \text{and} \tag{A4}$$

$$\nabla\cdot\mathbf{u} = 0, \tag{A5}$$

where $\mathbf{u} = (u, v, w)$ is the velocity vector and f is the Coriolis frequency. The effects of forcing and dissipation are represented by the schematic terms $\mathscr{F}$ and $\mathscr{D}$, respectively. Scalar C can be temperature T, salinity S, and nutrient concentration. The total density is split as $\rho(x, y, z, t) = \rho_r(z) + \rho_a(x, y, z, t)$, where the reference density ρ_r is generally chosen to be the time-mean and area-mean density and ρ_a is the perturbation density. The density transport can be derived from the T and S transport in Eqs. (A4) and the equation of state (von Storch et al. 2012). Applying the density decomposition yields

$$\frac{\partial \rho_a}{\partial t} + \mathbf{u} \cdot \nabla \rho_a = \frac{\rho_0 N^2}{g} w + \mathscr{F}_\rho + \mathscr{D}_\rho, \tag{A6}$$

where $\rho_0 = 1000\,\mathrm{kg\,m^{-3}}$ is the constant part of ρ_r, and the buoyancy frequency N is defined by

$$N^2 \equiv -\frac{g}{\rho_0}\frac{d\rho_r}{dz}. \tag{A7}$$

To obtain the mean flow and eddy energy equations, we separate a variable ϕ into its time-mean $\overline{\phi}$ and time-varying ϕ' parts. In particular, the densities of the four energy components ($\mathrm{J\,m^{-3}}$) are defined by

$$\mathrm{MKE} = E_{k0} = \frac{1}{2}\rho_0(\overline{u}^2 + \overline{v}^2), \tag{A8}$$

$$\mathrm{EKE} = \overline{E'_k} = \frac{1}{2}\rho_0\overline{(u'^2 + v'^2)}, \tag{A9}$$

$$\mathrm{MPE} = E_{p0} = \frac{g^2\overline{\rho}_a^2}{2\rho_0 N^2}, \quad \text{and} \tag{A10}$$

$$\mathrm{EPE} = \overline{E'_p} = \frac{g^2\overline{\rho'^2_a}}{2\rho_0 N^2}. \tag{A11}$$

The MKE (EKE) equation is obtained by multiplying the momentum equations in Eqs. (A1) and (A2) by $\rho_0\overline{u}$ ($\rho_0 u'$) and $\rho_0\overline{v}$ ($\rho_0 v'$), respectively, and then taking the time average of their sum to give

$$\frac{\partial E_{k0}}{\partial t} + \nabla \cdot \mathbf{F}_{k0} = C_m + C_{k0} + G_{k0} + \varepsilon_{k0}, \quad \text{and} \tag{A12}$$

$$\frac{\partial \overline{E'_k}}{\partial t} + \nabla \cdot \mathbf{F}'_k = C_e + C'_k + G'_k + \varepsilon'_k, \tag{A13}$$

where the advection ($\nabla \cdot \mathbf{F}$), conversion (C), and generation (G) terms are defined in Eqs. (3). Terms ε_{k0} and ε'_k represent the dissipation rates of MKE and EKE, respectively, due to friction and bottom drag. They are defined as

$$\varepsilon_{k0} = \overline{u}\,\overline{\mathscr{D}_u} + \overline{v}\,\overline{\mathscr{D}_v}, \quad \varepsilon'_k = \overline{u'\mathscr{D}'_u} + \overline{v'\mathscr{D}'_v}. \tag{A14}$$

The MPE and EPE equations are obtained by multiplying the density equation in Eq. (A6) by $g^2\overline{\rho_a}/\rho_0 N^2$ and $g^2\overline{\rho'_a}/\rho_0 N^2$, respectively, and then taking the time average to give

$$\frac{\partial E_{p0}}{\partial t} + \nabla \cdot \mathbf{F}_{p0} = -C_m + C_{p0} + G_{p0} + \varepsilon_{p0}, \quad \text{and} \tag{A15}$$

$$\frac{\partial \overline{E'_p}}{\partial t} + \nabla \cdot \mathbf{F}'_p = -C_e + C'_p + G'_p + \varepsilon'_p, \tag{A16}$$

where the advection, conversion, generation, and dissipation terms are defined as

$$\begin{aligned}
\nabla \cdot \mathbf{F}_{p0} &= \nabla \cdot (\overline{\mathbf{u}}E_{p0}),\\
\nabla \cdot \mathbf{F}_p{}' &= \nabla \cdot (\overline{\mathbf{u}E'_p}),\\
C_{p0} &= -\frac{g^2}{\rho_0 N^2}\overline{\rho_a}\nabla \cdot (\overline{\mathbf{u}'\rho'_a}),\\
C'_p &= -\frac{g^2}{\rho_0 N^2}\overline{\rho'_a\mathbf{u}'} \cdot \nabla\overline{\rho_a},\\
G_{p0} &= \frac{g^2}{\rho_0 N^2}\overline{\rho_a}\,\overline{\mathscr{F}_\rho},\\
G'_p &= \frac{g^2}{\rho_0 N^2}\overline{\rho'_a\mathscr{F}'_\rho},\\
\varepsilon_{p0} &= \frac{g^2}{\rho_0 N^2}\overline{\rho_a}\,\overline{\mathscr{D}_\rho},\\
\varepsilon'_p &= \frac{g^2}{\rho_0 N^2}\overline{\rho'_a\mathscr{D}'_\rho}.
\end{aligned} \tag{A17}$$

This set of energy equations provide an exact measurement of the four energy components in (A8)–(A11), their conversions (C terms) and dissipation (ε terms) within a given ocean domain, as well as their energy exchanges with external ocean ($\nabla \cdot \mathbf{F}$ terms) and atmosphere (G terms).

REFERENCES

Anderson, D. L. T., and R. A. Corry, 1985: Ocean response to low frequency wind forcing with application to the seasonal variation in the Florida Straits–Gulf Stream transport. *Prog. Oceanogr.*, **14**, 7–40, doi:10.1016/0079-6611(85)90003-5.

Brachet, S., P. Y. Le Traon, and C. Le Provost, 2004: Mesoscale variability from a high-resolution model and from altimeter data in the North Atlantic Ocean. *J. Geophys. Res.*, **109**, C12025, doi:10.1029/2004JC002360.

Carton, J. A., and B. S. Giese, 2008: A reanalysis of ocean climate using Simple Ocean Data Assimilation (SODA). *Mon. Wea. Rev.*, **136**, 2999–3017, doi:10.1175/2007MWR1978.1.

Chaigneau, A., A. Gizolme, and C. Grados, 2008: Mesoscale eddies off Peru in altimeter records: Identification algorithms and eddy spatio-temporal patterns. *Prog. Oceanogr.*, **79**, 106–119, doi:10.1016/j.pocean.2008.10.013.

Csanady, G. T., 1982: The thermohaline driving mechanism of oceanic jet streams. *J. Mar. Res.*, **40**, 113–142.

Duhaut, T. H., and D. N. Straub, 2006: Wind stress dependence on ocean surface velocity: Implications for mechanical energy input to ocean circulation. *J. Phys. Oceanogr.*, **36**, 202–211, doi:10.1175/JPO2842.1.

Ezer, T., and G. L. Mellor, 1992: A numerical study of the variability and the separation of the Gulf Stream, induced by surface atmospheric forcing and lateral boundary flows. *J. Phys. Oceanogr.*, **22**, 660–682, doi:10.1175/1520-0485(1992)022<0660:ANSOTV>2.0.CO;2.

Frankignoul, C., and P. Müller, 1979: Quasi-geostrophic response of an infinite β-plane ocean to stochastic forcing by the atmosphere. *J. Phys. Oceanogr.*, **9**, 104–127, doi:10.1175/1520-0485(1979)009<0104:QGROAI>2.0.CO;2.

Fu, L.-L., J. Vazquez, and M. E. Parke, 1987: Seasonal variability of the Gulf Stream from satellite altimetry. *J. Geophys. Res.*, **92**, 749–754, doi:10.1029/JC092iC01p00749.

Garnier, V., and R. Schopp, 1999: Wind influence on the mesoscale activity along the Gulf Stream and the North Atlantic currents. *J. Geophys. Res.*, **104**, 18 087–18 110, doi:10.1029/1999JC900070.

Gill, A. E., J. S. A. Green, and A. J. Simmons, 1974: Energy partition in the large-scale ocean circulation and the production of mid-ocean eddies. *Deep-Sea Res.*, **21**, 499–528, doi:10.1016/0011-7471(74)90010-2.

Hogg, N. G., 1992: On the transport of the Gulf Stream between Cape Hatteras and the Grand Banks. *Deep-Sea Res.*, **39**, 1231–1246, doi:10.1016/0198-0149(92)90066-3.

Jia, F., and L. Wu, 2011: Seasonal modulation of eddy kinetic energy and its formation mechanism in the Southeast Indian Ocean. *J. Phys. Oceanogr.*, **41**, 657–665, doi:10.1175/2010JPO4436.1.

Jouanno, J., J. Sheinbaum, B. Barnier, J. M. Molines, and J. Candela, 2012: Seasonal and interannual modulation of the eddy kinetic energy in the Caribbean Sea. *J. Phys. Oceanogr.*, **42**, 2041–2055, doi:10.1175/JPO-D-12-048.1.

Kang, D., and E. N. Curchitser, 2013: Gulf Stream eddy characteristics in a high-resolution ocean model. *J. Geophys. Res. Oceans*, **118**, 4474–4487, doi:10.1002/jgrc.20318.

——, and ——, 2015: Energetics of eddy–mean flow interactions in the Gulf Stream region. *J. Phys. Oceanogr.*, **45**, 1103–1120, doi:10.1175/JPO-D-14-0200.1.

Large, W. G., and S. G. Yeager, 2009: The global climatology of an interannually varying air-sea flux data set. *Climate Dyn.*, **33**, 341–364, doi:10.1007/s00382-008-0441-3.

LeTraon, P. Y., M. C. Rouquet, and C. Boissier, 1990: Spatial scales of mesoscale variability in the North Atlantic as deduced from Geosat data. *J. Geophys. Res.*, **95**, 20 267–20 285, doi:10.1029/JC095iC11p20267.

Müller, P., and C. Frankignoul, 1981: Direct atmospheric forcing of geostrophic eddies. *J. Phys. Oceanogr.*, **11**, 287–308, doi:10.1175/1520-0485(1981)011<0287:DAFOGE>2.0.CO;2.

Niiler, P. P., and W. S. Richardson, 1973: Seasonal variability of the Florida Current. *J. Mar. Res.*, **31**, 144–167.

Qiu, B., 1999: Seasonal eddy field modulation of the North Pacific Subtropical Countercurrent: TOPEX/Poseidon observations and theory. *J. Phys. Oceanogr.*, **29**, 2471–2486, doi:10.1175/1520-0485(1999)029<2471:SEFMOT>2.0.CO;2.

Rossby, T., C. Flagg, and K. Donohue, 2010: On the variability of Gulf Stream transport from seasonal to decadal timescales. *J. Mar. Res.*, **68**, 503–522, doi:10.1357/002224010794657128.

Ryan, J. P., J. A. Yoder, and D. W. Townsend, 2001: Influence of a Gulf Stream warm-core ring on water mass and chlorophyll distributions along the southern flank of Georges Bank. *Deep-Sea Res. II*, **48**, 159–178, doi:10.1016/S0967-0645(00)00117-X.

Scharffenberg, M. G., and D. Stammer, 2010: Seasonal variations of the large-scale geostrophic flow field and eddy kinetic energy inferred from the TOPEX/Poseidon and Jason-1 tandem mission data. *J. Geophys. Res.*, **115**, C02008, doi:10.1029/2008JC005242.

Shchepetkin, A. F., and J. C. McWilliams, 2003: A method for computing horizontal pressure-gradient force in an oceanic model with a nonaligned vertical coordinate. *J. Geophys. Res.*, **108**, 3090, doi:10.1029/2001JC001047.

——, and ——, 2005: The Regional Oceanic Modeling System: A split-explicit, free-surface, topography-following-coordinate ocean model. *Ocean Modell.*, **9**, 347–404, doi:10.1016/j.ocemod.2004.08.002.

Spall, M. A., and A. R. Robinson, 1990: Regional primitive equation studies of the Gulf Stream meander and ring formation region. *J. Phys. Oceanogr.*, **20**, 985–1016, doi:10.1175/1520-0485(1990)020<0985:RPESOT>2.0.CO;2.

Stammer, D., and C. Wunsch, 1999: Temporal changes in eddy energy of the oceans. *Deep-Sea Res. II*, **46**, 77–108, doi:10.1016/S0967-0645(98)00106-4.

——, C. Boning, and C. Dieterich, 2001: The role of variable wind forcing in generating eddy energy in the North Atlantic. *Prog. Oceanogr.*, **48**, 289–311, doi:10.1016/S0079-6611(01)00008-8.

Stommel, H., 1965: The Gulf Stream: A Physical and Dynamical Description. 2nd ed. University of California Press, 248 pp.

Teague, W. J., and Z. R. Hallock, 1990: Gulf Stream path analysis near the New England Seamounts. *J. Geophys. Res.*, **95**, 1647–1662, doi:10.1029/JC095iC02p01647.

The Ring Group, 1981: Gulf Stream cold-core rings: Their physics, chemistry, and biology. *Science*, **212**, 1091–1100, doi:10.1126/science.212.4499.1091.

von Storch, J.-S., C. Eden, I. Fast, H. Haak, D. Hernandez-Deckers, E. Maier-Reimer, J. Marotzke, and D. Stammer, 2012: An estimate of the Lorenz energy cycle for the World Ocean based on the 1/10° STORM/NCEP simulation. *J. Phys. Oceanogr.*, **42**, 2185–2205, doi:10.1175/JPO-D-12-079.1.

White, M. A., and K. Heywood, 1995: Seasonal and interannual changes in the North Atlantic subpolar gyre from Geosat and TOPEX/Poseidon altimetry. *J. Geophys. Res.*, **100**, 24 931–24 941, doi:10.1029/95JC02123.

Worthington, L. V., 1976: *On the North Atlantic Circulation.* Johns Hopkins University Press, 110 pp.

Yang, J., 2015: Local and remote wind stress forcing of the seasonal variability of the Atlantic Meridional Overturning Circulation (AMOC) transport at 26.5°N. *J. Geophys. Res. Oceans*, **120**, 2488–2503, doi:10.1002/2014JC010317.

Zhai, X., and R. J. Greatbatch, 2006: Surface eddy diffusivity for heat in a model of the northwest Atlantic Ocean. *Geophys. Res. Lett.*, **33**, L24611, doi:10.1029/2006GL028712.

——, ——, and J.-D. Kohlmann, 2008: On the seasonal variability of eddy kinetic energy in the Gulf Stream region. *Geophys. Res. Lett.*, **35**, L24609, doi:10.1029/2008GL036412.